crystals

MDPI

Article

The Spinodal Decomposition of Ferrite in 2507 Biphasic Stainless Steels: Embrittlement and Possible Toughness Recovery

Barbara Rivolta [1], Riccardo Gerosa [1,*], Davide Panzeri [1], Enrico Mariani [2] and Francesca Tavasci [3]

[1] Department of Mechanical Engineering, Politecnico di Milano, Via La Masa 1, 20156 Milan, Italy; barbara.rivolta@polimi.it (B.R.); davide.panzeri@polimi.it (D.P.)
[2] SMT S.r.l., Via del Lavoro, 3, 20060 Pozzo d'Adda, Italy
[3] Tecnofar S.p.A., Via al Piano, 54 A, 23020 Gordona, Italy
* Correspondence: riccardo.gerosa@polimi.it

Abstract: Biphasic stainless steels provide an excellent combination of mechanical and corrosion properties. The occurrence of ferrite spinodal decomposition during processing and heat treatment can induce a dramatic drop in impact energy. In this paper, a forged rod of 480 mm diameter made of 2507 biphasic stainless steel was studied. The spinodal decomposition phenomenon upon aging at 475 °C (748 K) was investigated by macro- and micro-hardness tests on the constituent phases and by Charpy impact tests. Then, the influence of the microstructural constituents and their morphology on the crack path was studied by optical microscopy, noting possible correlations with the impact energy. Successively, the fracture surfaces of selected specimens were analyzed by a scanning electron microscope (SEM). Finally, reversion heat treatments at 550 °C (823 K) and 600 °C (873 K) were investigated to evaluate the possibility of recovering the detrimental effects of the α' embrittlement. According to the literature, this procedure works well with some biphasic steels, but these steels are characterized by a chromium content lower than that of 2507 grade steel. Regarding the 2507 grade steel studied in this work, complete reversion was obtained by solution-annealing treatment, while reversion heat treatments at both 600 °C (873 K) and 550 °C (823 K) allowed only a partial recovery.

Keywords: super duplex stainless steels; 475 °C embrittlement; transition curve; crack path; fractography

Citation: Rivolta, B.; Gerosa, R.; Panzeri, D.; Mariani, E.; Tavasci, F. The Spinodal Decomposition of Ferrite in 2507 Biphasic Stainless Steels: Embrittlement and Possible Toughness Recovery. *Crystals* **2023**, *13*, 1424. https://doi.org/10.3390/cryst13101424

Academic Editors: Xin Xu, Ziyong Hou, Lijun Wang and Peter Hedström

Received: 5 September 2023
Revised: 20 September 2023
Accepted: 24 September 2023
Published: 25 September 2023

1. Introduction

Super duplex stainless steels are well known for their excellent mechanical properties, corrosion resistance, and low-temperature toughness. For these reasons, they are commonly employed in the industrial world, mainly in the oil and gas field, for high-demanding applications. These outstanding potentialities are related to a rich and complicated chemical composition that requires careful control of the high-temperature deformation and the heat-treating parameters. In fact, a wide and complex precipitation response upon thermal exposure above approximately 300 °C (573 K), with the formation of detrimental embrittling phases, characterize such alloys [1–5]. For this reason, their employment in service conditions associated with high temperatures is not recommended. For example, limitations on the service temperature are prescribed for boilers and pressure vessels because of the high reduction in toughness. Regarding the F55 steel grade, both the VdTÜV standards and the American Society of Mechanical Engineers (ASME) Boiler and Pressure Vessel Code recommend a maximum service temperature of 250 °C (523 K) [6]. Among the precipitation phenomena, the spinodal decomposition of ferrite is particularly critical in the temperature range from 300 °C (573 K) to 500 °C (773 K).

Since the phenomenon kinetic is faster at about 475 °C (748 K), it is also known as "475 °C (748 K) embrittlement" [7,8]. The spinodal decomposition of ferrite is related to a local atomic reorganization of iron (Fe) and chromium (Cr), leading to the formation of clusters in ferrite with a wide fluctuation in the local content of these elements. This phenomenon decomposes the ferrite in the Fe-rich α and Cr-rich α' regions [7,8]. The

occurrence of such deleterious transformations can be detected not only by impact testing, but also by a micro-hardness test. In fact, such testing determines a huge toughness loss, together with a significant increase in ferrite hardness, which is related to the mismatch of the elastic moduli and the lattice parameters between the α and α' phases [7,8]. Sufficiently long exposure in both isothermal and anisothermal conditions within the critical temperature interval can be obtained not only during heat treatment and processing, but also during service.

Regarding the heat treatments, the cooling of large components from the solution-annealing temperature can be slow enough to activate undesired precipitation phenomena, such as spinodal decomposition. For this reason, the heat-treatment parameters should be carefully controlled and optimized, not only in terms of solution temperature and heating time, but also in terms of cooling rates. Nevertheless, considering the low conductivity of such materials, the presence of detrimental phases cannot be excluded for large components. The spinodal decomposition could also affect welded parts. In fact, in the welding process, the thermal cycle influences the microstructure in both the melted and the heat-affected zones. In general, if the welding process is not carefully designed and carried out, an unbalanced microstructure may result and precipitation of secondary phases may occur [9,10]. For this reason, as specified by welding recommendations for duplex stainless steels, the welding procedure must be carefully controlled, especially in terms of cooling rates, interpass temperature, and heat input. Moreover, preheating and post-heating are generally not recommended, especially for these steel grades [9,10], and the interpass temperature is normally limited to about 100 °C (373 K) to enhance the cooling process. When the required microstructural balance and/or the absence of secondary phases cannot be ensured, a solution-annealing treatment is mandatory [9,10].

The occurrence of deleterious phenomena can also be caused by the incompatibility of the material with the service conditions or the presence of overheating with respect to the standard operative parameters. In the technical literature [8,11,12], some researchers studied possible methods to recover the mechanical properties and the microstructural features after the occurrence of 475 °C (748 K) embrittlement. One of the proposals involved "reversion" heat treatments from 550 °C (823 K) to 600 °C (873 K). In fact, since this temperature interval is above the $\alpha - \alpha'$ miscibility gap in the Fe-Cr system, the decomposition become thermodynamically unstable, leading to dissolution of the α' phase within α-ferrite [8,11,12]. For instance, according to the literature [11], in the steel grade UNS S32205, which contains less chromium than UNS S32760, the maximum recommended duration of the reversion treatment at 550 °C (823 K) is 60 min [11,12]. If the time in this temperature range exceeds this limit, several detrimental intermetallic phases, such as R, secondary austenite, χ, and σ phases, could precipitate within ferrite [8,11,12]. For this reason, as described in the literature [8,11,12], the reversion heat treatment does not allow a complete reversion of the initial pre-embrittlement mechanical properties. In addition, a reversion heat treatment at temperatures above 600 °C (873 K) is not recommended because of the formation of other detrimental secondary phases after very short times. This is clearly explained by the isothermal precipitation diagram in Figure 1.

In this study, the modifications induced by the spinodal decomposition of ferrite are investigated by macro-hardness and micro-hardness tests and by Charpy impact tests, varying the soaking time at 475 °C (748 K). The crack path and its relationship with the microstructure are studied by optical microscopy. Since the harmful effects of such embrittlement can be deleted by a solution-annealing treatment, the toughness recovery at 1120 °C (1393 K) is studied, varying the soaking time. Then, the recovery of the material properties by reversion heat treatments from 550 °C (823 K) to 600 °C (873 K) is investigated. Finally, the fracture surfaces are analyzed by a scanning electron microscope (SEM) to study the fracture micro-mechanisms.

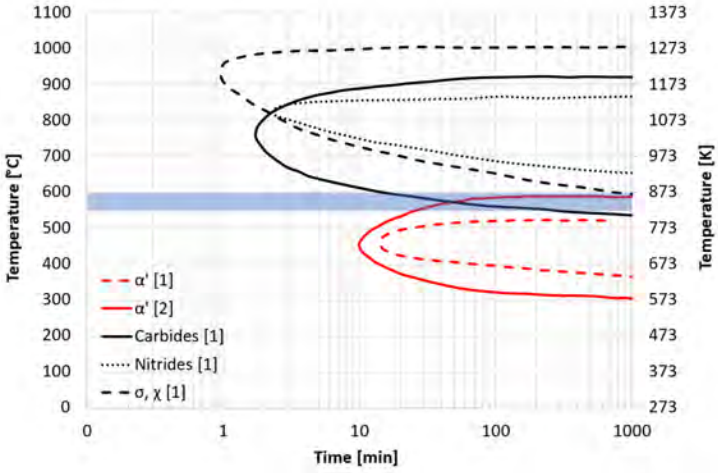

Figure 1. Time-temperature precipitation curves for F55 grade steel [1,2]. The blue area represents the temperature range from 550 °C (823 K) to 600 °C (873 K) adopted for the recovery heat treatments investigated in this study.

2. Materials and Methods

We studied a commercial cylindrical rod with diameter equal to 480 mm and length equal to 70 mm. It was made of ferritic-austenitic F55-grade steel (UNS S32760) provided in as-forged condition. The chemical composition of the material adopted in this study is reported in Table 1. It is compatible with the compositional limits prescribed by the ASTM A182/A182M standard specification and by the Norsk Sokkels Konkuranseposisjon (NORSOK) standards [13,14]. The chemical composition analysis was performed by optical emission spectroscopy using a Horiba–Jobin Yvon OES spectrometer on samples taken close to the sampling positions of the Charpy V-notch specimens.

Table 1. Average chemical composition. Content of alloying elements in wt. % in the alloy investigated in this study (Fe bal.).

	C	Mn	Si	Cr	Ni	Mo	Cu	N	W	S	P
wt. %	0.03	0.66	0.51	25.80	7.10	3.70	0.59	0.29	0.64	0.001	0.02

Samples (15 mm × 60 mm × 70 mm) were taken from the circumferential direction, as shown in Figure 2. They were solution-annealed at 1120 °C (1393 K) and water-quenched according to the ASTM A182/A182M standard and the NORSOK standards [13,14]. Some of them were successively cut into two halves (from each half, three Charpy V-notch specimens can be machined) and aged at 475 °C (748 K) for times between 15 min and 360 min. The samples for the investigation of reversion heat treatments were characterized by dimensions of 5 mm × 5 mm × 10 mm.

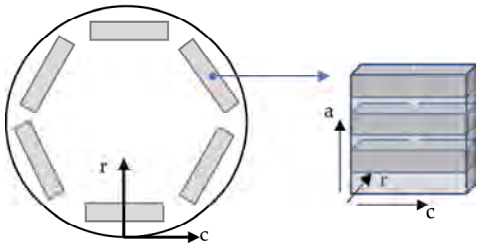

Figure 2. Sampling positions of the Charpy V-notch specimens from the original rod. The radial (r), the circumferential (c) and the axial (a) directions are reported.

The as-solution annealed material was characterized from the metallographic point of view and the distributions of the austenite spacing and the size of austenite islands

were investigated by light optical microscopy at 50× magnification. The average size and the standard deviation in each direction and the overall mean values were determined in accordance with the ASTM E112 [15] standard.

All the heat treatments were carried out using a laboratory Carbolite (model CWF13/13) chamber furnace. After metallographic preparation, according to the conventional technique, the samples were electrolytically etched in a KOH solution 10N for microstructural analysis in accordance with the ASTM E407 [16] standard. In particular, samples were cut using silicon carbide cut-off wheels with a Remet (model TR100 EV) cutting machine. Mounting was performed in hot thermo-setting phenolic resin using a Metkon (model Ecopress 50) mounting machine. Grinding and polishing were carried out using a Struers (model Pedemax 2 + Planopol 3) machine, up to mirror-polished condition. After that, electrolytic etching was performed, adopting a voltage range from 2 V to 3 V and a time between 10 s and 15 s, depending on the sample size. A Leica (model DMR) light optical microscope and a Zeiss (modelSIGMA 500) scanning electron microscope were adopted for the metallographic and fractographic analyses. The austenite-to-ferrite ratio was determined by image analysis on optical micrographs at 50× magnification. In order to study the influence of the spinodal decomposition on ferrite and austenite, the hardness of each constituent phase was measured by a Vickers micro-hardness test, adopting a load of 0.05 kgf (HV0.05). The Vickers HV30 macro-hardness was also measured in each condition to study the influence of the spinodal decomposition on the bulk properties. Hardness tests were carried out using a Future Tech (model FM 700) micro-hardness tester and a Wolpert (model Testor 930) macro-hardness tester according to the standard EN ISO 6507 standard [17]. The impact energy, in both the solution-annealed and aged conditions, was determined by Charpy V-notch impact testing, using a Wolpert Charpy pendulum according to the NORSOK standard, the ASTM A370 standard, and the ASTM E23 standard [14,18,19]. The test temperature was controlled with a cryogenic cell. The NORSOK standard prescribes a minimum average absorbed energy of 45 J (35 J single), with Charpy V-notch impact tests performed at −46 °C (227 K) [14]. In each condition, three impact tests were performed. Then, the crack paths were studied in selected conditions, cutting the impact specimen along a plane perpendicular to the notch and positioned at half thickness. In each condition, the total crack length from the notch tip was measured and compared to the nominal length of 8 mm. As shown in Figure 3, the crack path can involve intra-ferrite, intra-austenite, and interphase regions. Since the last contribution is often not easily distinguishable from the intra-ferrite fraction, these contributions to the crack propagation path are summarized in a unique value in this study. Clearly, high absorbed energy is associated with a large intra-austenite propagation. Finally, the fracture surfaces of the Charpy impact specimens, which were adopted to investigate both the spinodal embrittlement upon aging at 475 °C (748 K) and the ductile-to-brittle transition curve of the as-solution annealed material, were analyzed by SEM.

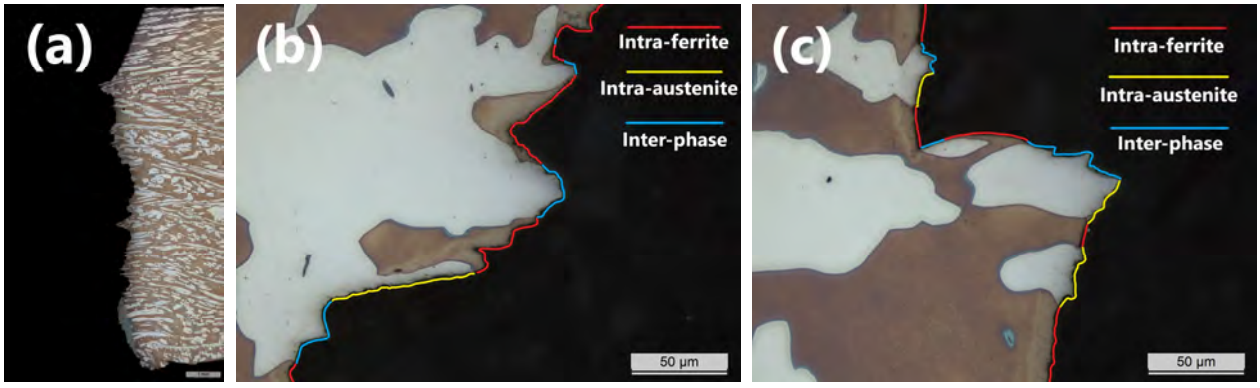

Figure 3. Crack propagation in the Charpy impact specimens. Overview of the overall crack path obtained after sectioning the Charpy specimen at half thickness (**a**). Types of microstructural constituents along the crack path: intra-austenite, intra-ferrite, and interphase (**b**) (Example 1) and (**c**) (Example 2).

3. Results

In the solution-annealed condition, the microstructure analyzed by optical microscopy was free of undesired intermetallic secondary phases, as required by the NORSOK standard [14]. The ferrite fraction was equal to 54.5% and it was calculated in accordance with the ASTM E562 standard [20]. It is compatible with the range prescribed by the NORSOK standard [14]. Figure 4 shows the micrographs obtained at the light-optical microscope of the microstructure in the solution-annealed condition. The distributions of the austenite spacing and the size of austenite islands were determined on optical micrographs at 50× magnification, considering the radial, circumferential and longitudinal directions of the cylindrical rod. The average and the standard deviation in each direction of both the austenite spacing and the austenite size are shown in Table 2. The global mean values were calculated via Equation (1).

$$d = \sqrt[3]{d_r d_l d_\theta} \quad (1)$$

where d_r, d_l and d_θ represent the average radial, longitudinal, and circumferential sizes, respectively. Moreover, the related distribution histograms in all the directions are shown in Figure 5.

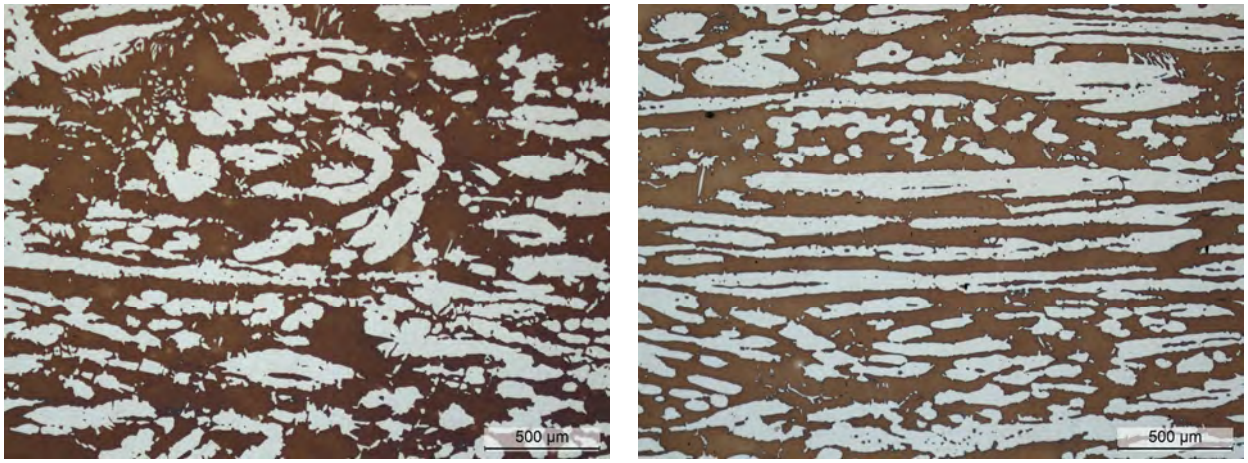

(**a**) (**b**)

Figure 4. Microstructure in the solution-annealed condition. Optical micrographs at 50× magnification: (**a**) radial–circumferential plane; (**b**) radial–longitudinal plane.

The investigation of the austenite spacing and the size of austenite islands is very important because they can influence the mechanical properties, such as toughness and fatigue resistance, as well as some microstructural features, such as nitrides precipitation. In fact, as reported in the literature [3,21,22], the presence of a finer austenite spacing implies shorter nitrogen diffusion distances from the core of ferrite grains to the adjacent austenite, thus reducing nitrides precipitation in ferrite. Fine austenite and ferrite grain sizes are also important to improve toughness, especially when the spinodal decomposition is adopted as the strengthening mechanism. In fact, the technical literature reports some experimental works that were aimed at improving the static and dynamic properties of duplex stainless steels, exploiting the hardening effect of the α' phase [23,24]. The main drawback was the well-known toughness decrease that can be limited by grain refinement and suitable orientation of the microstructure [25]. The analysis shown in Figure 5 and the data reported in Table 2 demonstrate that, in the longitudinal direction, the austenite islands are longer. Therefore, cracks propagating in the radial-circumferential plane find greater resistance than the cracks propagating in the other directions.

Table 2. Austenite spacing (AS) and size of austenite islands (AI). Average values and standard deviations in the solution-annealed material as functions of the direction and overall mean values.

	Radial		Longitudinal		Circumferential		Global	
	AS	**AI**	**AS**	**AI**	**AS**	**AI**	**AS**	**AI**
Average [µm]	62	55	141	140	85	79	90	85
Standard deviation [µm]	54	37	115	93	77	7	75	29

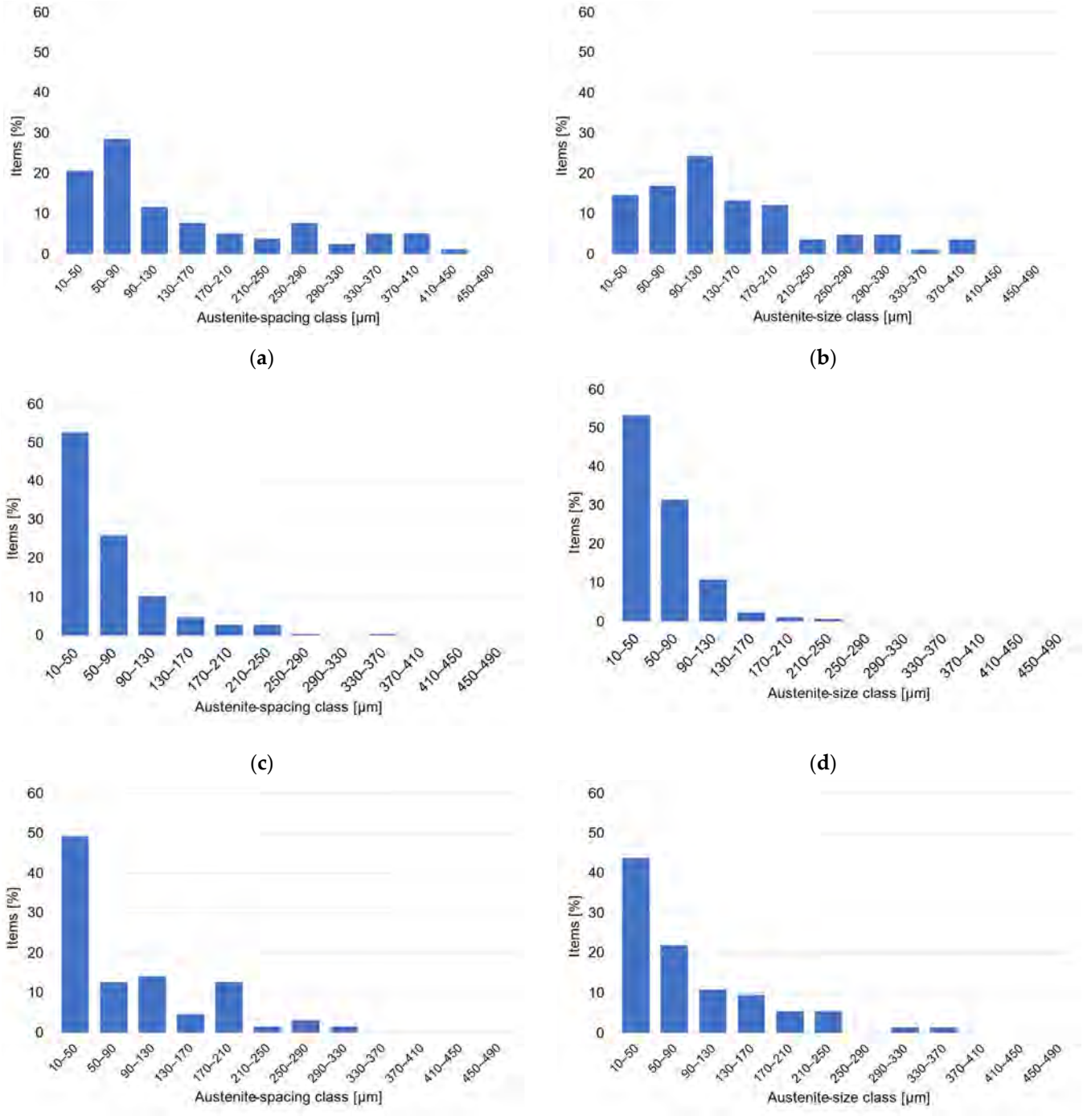

Figure 5. Distributions of the austenite spacing and the size of austenite islands in the solution-annealed material: (**a**,**b**) refer to the longitudinal direction, (**c**,**d**) refer to the radial direction, (**e**,**f**) refer to the circumferential direction.

Then, as reported in Table 3, the micro-hardness of each constituent phase (ferrite and austenite) was measured in the solution-annealed condition, together with the macro-hardness. In the solution-annealed condition, the Charpy impact energy at −46 °C (227 K) was also determined, as reported in Table 3. The impact energy at −46 °C (227 K) is compatible with respect to the minimum value prescribed by the NORSOK standard [14]. The acceptable impact energy value confirms the efficacy of the solution-annealing treatment in removing all the undesired and embrittling phases, including the spinodal decomposition of ferrite.

Table 3. Vickers micro-hardness and macro-hardness values and impact energy at −46 °C (227 K) in the solution-annealed condition.

	HV0.05 Ferrite	**HV0.05 Austenite**	**HV30**	**$KV_{-46\,°C}$ [J]**
Average	302	261	254	160
Standard deviation	4	5	6	23

Then, the influence of the ferrite spinodal decomposition on the mechanical properties was investigated by hardness tests and Charpy impact tests on samples solution-annealed at 1120 °C (1393 K) and aged at 475 °C (748 K) from 15 min to 360 min. The micro-hardness of both the constituent phases (ferrite and austenite) was measured in each aging condition, together with the bulk macro-hardness. The ferrite spinodal decomposition did not provide any appreciable variation of the austenite micro-hardness. The variation of the macro- and micro-hardness as function of the aging time at 475 °C (748 K) are shown in Figure 6. Successively, the influence of the spinodal decomposition of ferrite on the impact energy at −46 °C (227 K) was also investigated in each aging condition. The results are reported in Figure 6.

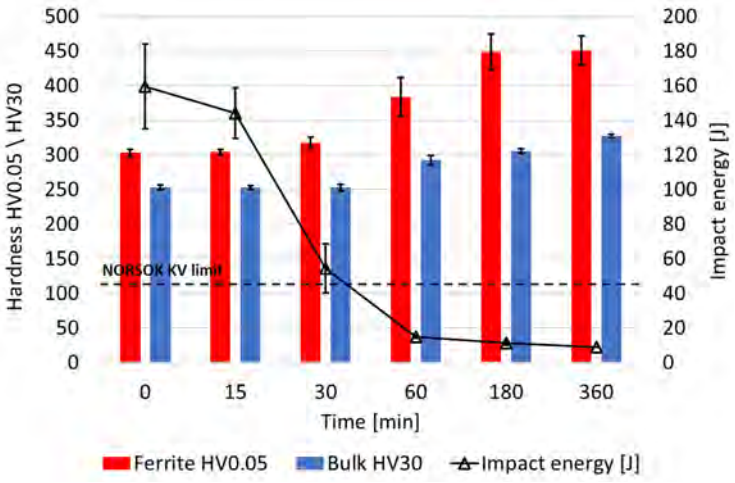

Figure 6. Bulk macro-hardness HV30, ferrite micro-hardness HV0.05, and impact energy at −46 °C (227 K) as functions of the aging time at 475 °C (748 K). The black dashed line represents the minimum impact energy at −46 °C (227 K), prescribed by the NORSOK standard [14].

Then, the crack propagation path on the Charpy impact specimens was investigated, measuring both the total crack length and the percentage amounts of each constituent phase (intra-austenite and intra-ferrite/interphase propagation). This analysis was performed to investigate the interaction between the propagating crack and the microstructure, especially in the presence of very low impact-energy values. The obtained results in each condition are reported in Table 4. The crack length was measured from the notch tip.

Table 4. Total crack length and percentage amounts of each microstructural constituent in the Charpy impact specimens.

Aging Time [min]	Total Crack Length [mm]	Intra-Ferrite/Interphase [%]	Intra-Austenite [%]
0	13.5	83	17
30	13.8	80	20
60	13.9	81	19
360	12.3	83	17

Then, the fracture surfaces of the Charpy impact specimens were investigated by SEM in both the solution-annealed and aged conditions. The SEM micrographs are reported in Figure 7.

The impact-energy loss at −46 °C (227 K) related to the spinodal decomposition of ferrite, varying the aging times, was compared with the impact-energy reduction due to the decrease in the test temperature in the solution-annealed condition. For this reason, the ductile-to-brittle transition curve in the as-solution annealed condition was determined by Charpy impact tests, varying the test temperature from 20 °C (293 K) to −80 °C (193 K). The ductile-to-brittle transition curve is shown in Figure 8. The tested material satisfied the minimum NORSOK requirement of 45 J as the average impact-energy at −46 °C (227 K) [14]. The average margin was 114 J. This material was characterized by impact energy higher than 45 J even at lower temperatures. The average margins were 16 J at −70 °C (203 K) and 4 J at −80 °C (193 K). Finally, the ductile-to-brittle transition temperature in the as-solution annealed condition was calculated, considering the amount of ductile area in the Charpy specimens according to ASTM A370-21 standard [18]. Its value was equal to −37 °C (236 K) and it corresponded to the temperature at which 50% shear area was present.

Considering the ductile-to-brittle transition curve reported in Figure 8, it is possible to state that the impact-energy loss in the as-solution annealed material, obtained by reducing the test temperature, is not as detrimental as that induced by the spinodal decomposition phenomenon.

The crack propagation path was investigated in each Charpy impact specimens adopted to determine the ductile-to-brittle transition curve. Both the total crack length and the percentage amounts of each constituent phase (intra-austenite and intra-ferrite/interphase propagation) were measured. The obtained results are shown in Table 5. The crack path was measured from the notch tip on the half-thickness plane.

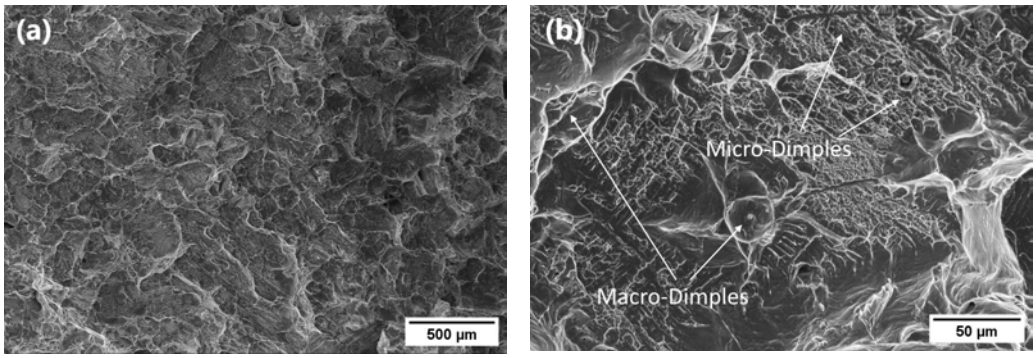

Figure 7. *Cont.*

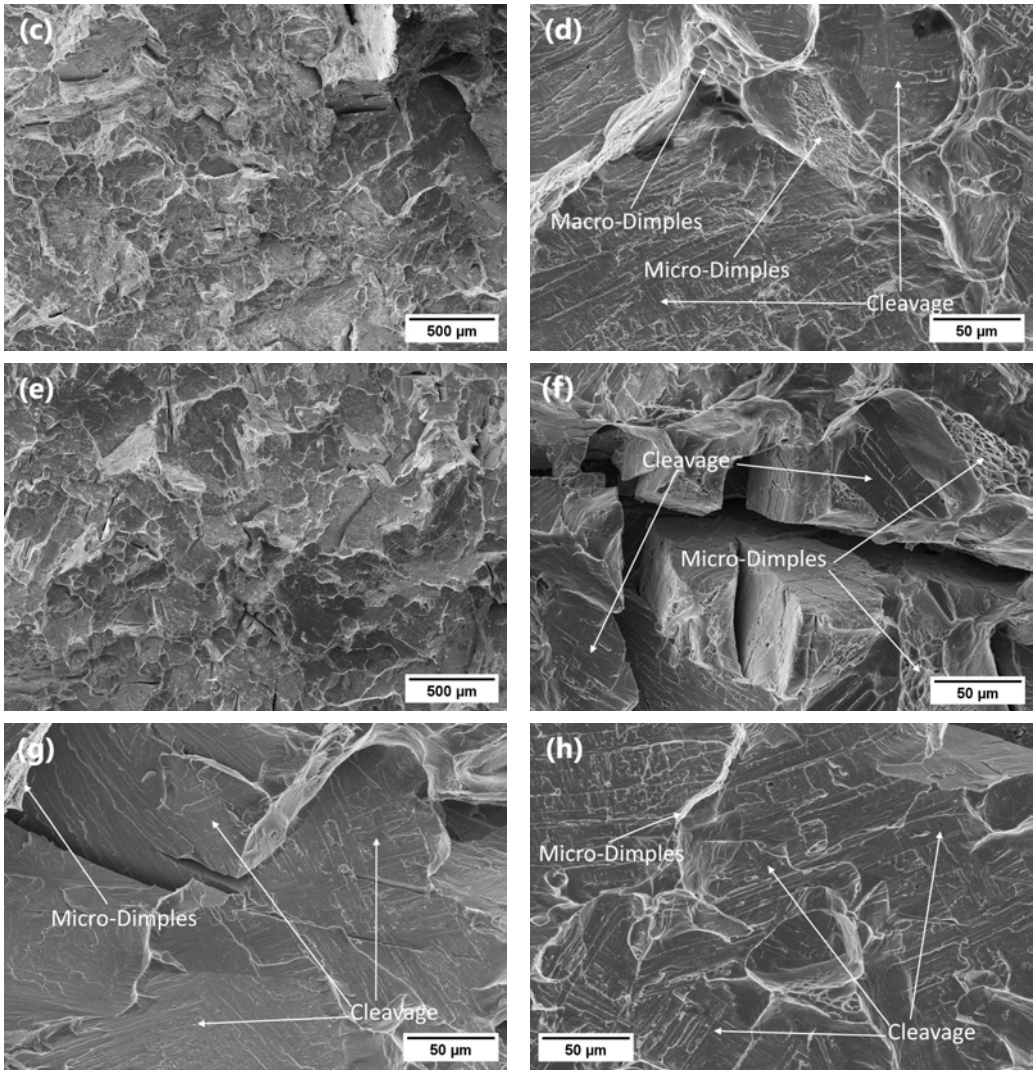

Figure 7. SEM micrographs obtained with a secondary electrons signal. Fracture surfaces of the Charpy impact specimens with different magnifications: (**a**,**b**) as-solution annealed condition; (**c**,**d**) 475 °C (748 K) 30 min; (**e**,**f**) 475 °C (748 K) 60 min; (**g**) 475 °C (748 K) 180 min; (**h**) 475 °C (748 K) 360 min.

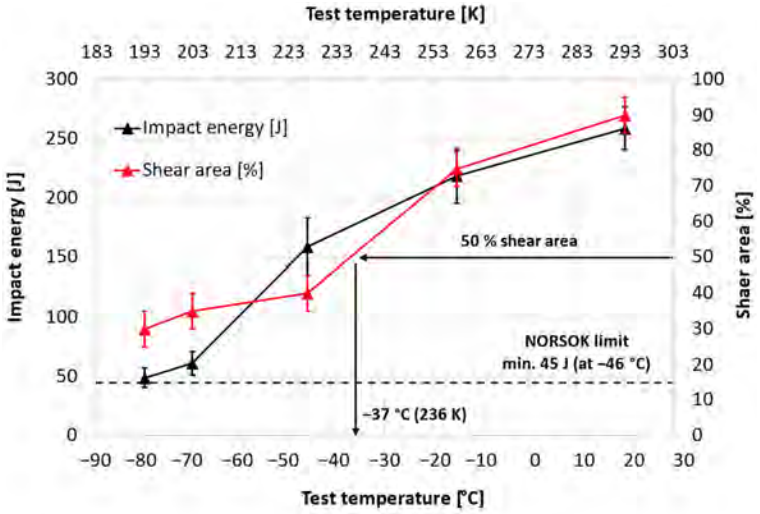

Figure 8. Ductile-to-brittle transition curve and shear area of the investigated F55 grade in the as-solution annealed condition.

Table 5. Total crack length and percentage amounts of each microstructural constituent in the Charpy impact specimens of the ductile-to-brittle transition curve.

Test Temperature [°C]	Total Crack Length [mm]	Intra-Ferrite/Interphase [%]	Intra-Austenite [%]
−80 (193 K)	12.6	81	19
−70 (203 K)	12.3	79	21
−46 (227 K)	11.3	80	20
−15 (258 K)	14.2	81	19
20 (293 K)	12.3	91	9

Then, the fracture surfaces of the Charpy impact specimens were investigated by SEM. The SEM micrographs are shown in Figure 9.

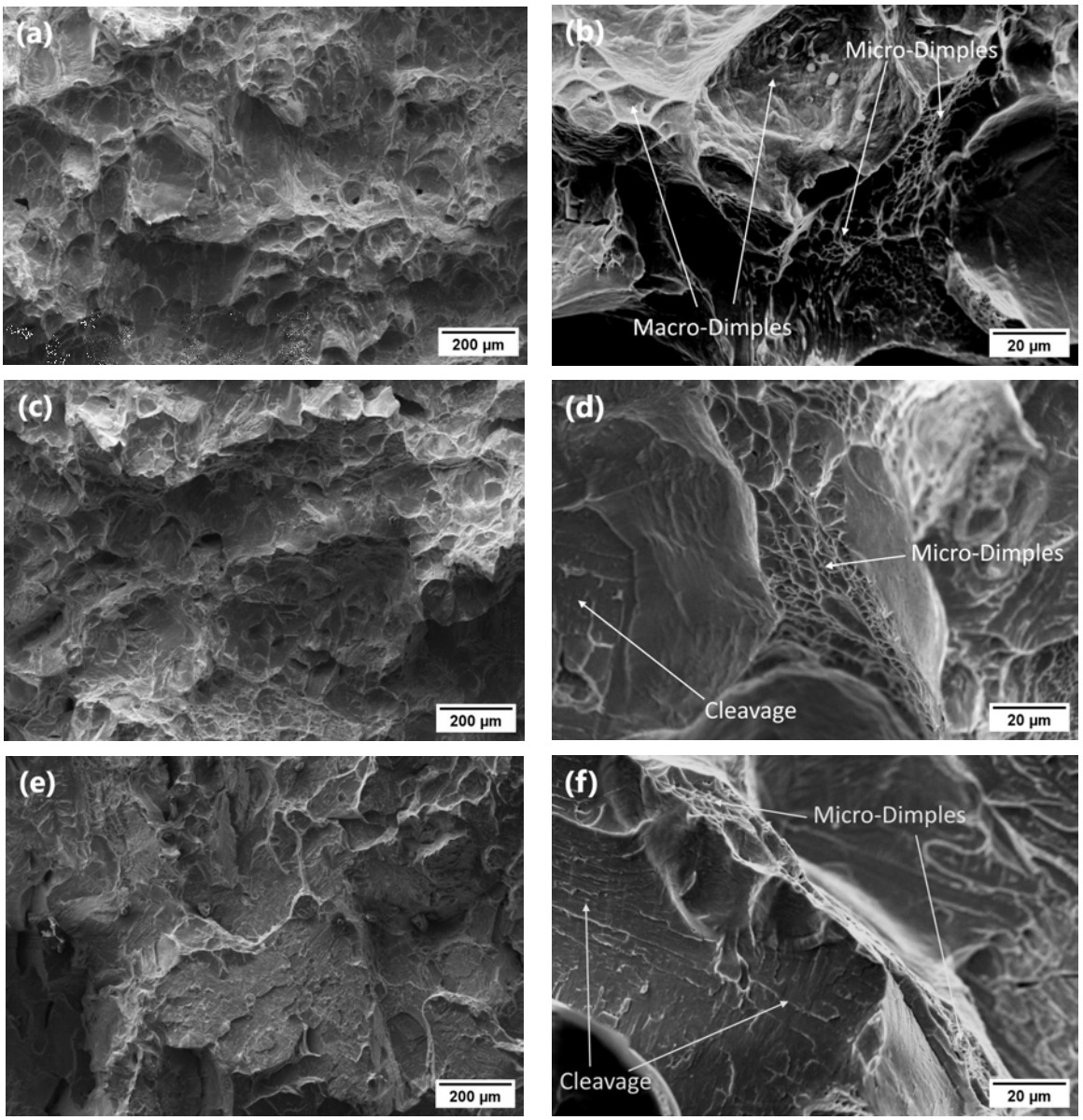

Figure 9. SEM micrographs obtained with a secondary electrons signal. Fracture surfaces of the Charpy impact specimens in the as-solution annealed condition adopted to determine the ductile-to-brittle transition curve: (**a**,**b**) 20 °C (293 K); (**c**,**d**) −46 °C (227 K); (**e**,**f**) −80 °C (193 K).

As suggested by the data shown in Tables 4 and 5, the crack propagation follows the weaker microstructure, i.e., ferrite, in both the as-solution annealed and embrittled conditions. This is compatible with the fact that austenite properties are not affected by the spinodal decomposition. Therefore, crack propagation in the austenite islands of the embrittled specimens requires high energy, such as the energy in the as-solution annealed condition.

The severe drawbacks related to spinodal decomposition encouraged the metallurgical researchers to investigate and develop possible recovery heat treatments after the 475 °C (748 K) embrittlement. Shamanth et al. [11] reported positive results in the recovery of 2205 duplex stainless steel, while Li et al. [26] proposed a successful treatment to improve the ductility of Z3CN20-09M steel. Both steels have chromium content lower than that of the 2507 steel. Therefore, we planned an experimental campaign to study whether beneficial effects can also be obtained with a higher-chromium grade steel. As shown in Figure 10, after re-solution annealing at 1120 °C (1393 K), the ferrite micro-hardness was already fully recovered, after 10 min, to the pre-embrittlement values. In this condition, the impact energy at −46 °C (227 K) resulted equal to 149 J. These results confirmed the efficacy of the re-solution annealing treatment at 1120 °C (1393 K) in recovering the detrimental effects of the spinodal decomposition of ferrite.

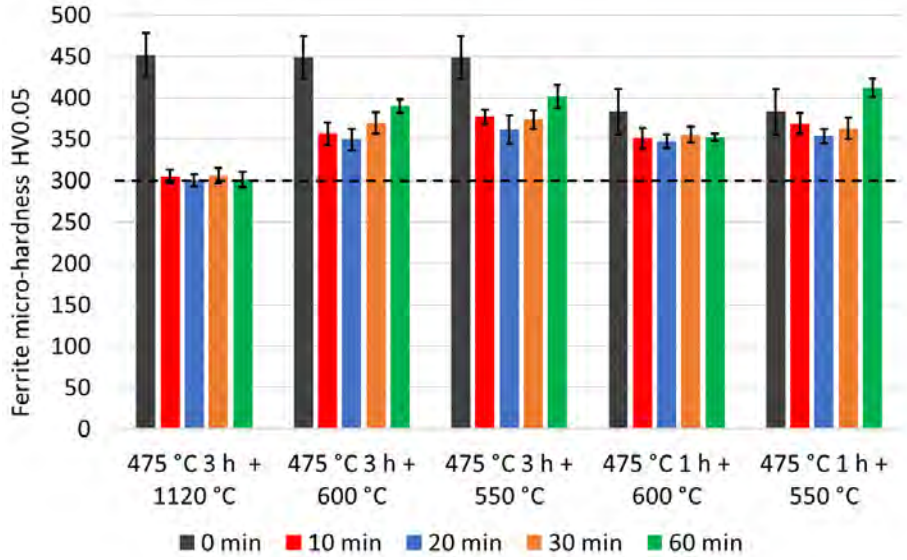

Figure 10. Recovery heat treatments. Vickers HV0.05 ferrite micro-hardness as a function of the recovery time at 550 °C (823 K), 600 °C (873 K), and 1120 °C (1393 K). The black dashed line represents the ferrite micro-hardness in the as-solution annealed condition before the 475 °C (748 K) aging embrittlement. The error bars are symmetric and represent the standard deviation.

After that, recovery heat treatments at both 550 °C (823 K) and 600 °C (873 K) were investigated. At both temperatures, the ferrite micro-hardness was slightly reduced after 10 min. Longer exposures did not provide further hardness reduction, and after 1 h, hardness started increasing again. Before the exposures investigated in this study, the reversion heat treatments at both 600 °C (873 K) and 550 °C (823 K) did not determine any precipitation of carbides and intermetallic phases observable via light-optical or scanning-electron microscopes. The hardness increment after 60 min was probably determined by the intersection of the spinodal decomposition curve, as shown in Figure 1. This confirmed that exposures longer than 30 min are not feasible at these temperatures because of the re-activation of the spinodal decomposition phenomenon.

4. Discussion

The spinodal decomposition of ferrite determined a selective ferrite hardening, as demonstrated by the micro-hardness curves shown in Figure 6. Such a phenomenon did not affect the austenite phase, in which micro-hardness remained constant with increasing

aging time. Up to 30 min aging, the ferrite micro-hardness remained close to the as-solution annealed value. It was subjected to a steep increase after 1 h and the steady-state value of about 450 HV0.05 was obtained at 3 h. At this time, the ferrite micro-hardness was increased by approximately 49%, compared to the solution-annealed condition. In general, the ferrite micro-hardness was strongly dependent on decomposition uniformity and crystallographic orientation. Such dependence justified the large scattering of the ferrite micro-hardness. Regarding the bulk macro-hardness, its increment was delayed compared to that of the ferrite micro-hardness. In fact, it remained constant up to 1 h and then it increased. Such delay depended on the fact that the macro-hardness imprint involves not only ferrite, but also austenite in an average proportion defined by the measured austenite/ferrite ratio. Therefore, the macro-hardness test is less effective in detecting the beginning of the hardening phenomenon.

The selective ferrite hardening determined by the spinodal decomposition was obtained at the expense of an increasing embrittlement. In fact, as shown by the experimental results shown in Figure 6, the impact energy quickly decreased with increasing aging time. After 1 h, the embrittling effect was no longer compatible with the minimum NORSOK requirements [14]. At this time, the impact energy of 15 J corresponded to a reduction of 91%, compared to the as-solution annealed condition. The influence of the spinodal decomposition on the impact energy was observed earlier than the effect on the ferrite micro-hardness. In fact, after 30 min, the impact energy (54 J) was subjected to a dramatic loss, with a reduction of 66% compared to that of the as-solution annealed condition. On the other hand, the ferrite micro-hardness was only slightly increased, at about 5%, and the bulk macro-hardness remained constant. Such a difference suggested that the impact test was more effective than both the ferrite micro-hardness and the bulk macro-hardness in determining the beginning of spinodal decomposition.

To better investigate the increase in ferrite micro-hardness, the process fractions, $X_{HV}(t)$, were determined, according to Equation (2). The impact-energy loss was similarly studied, calculating the process fractions, $X_{KV}(t)$, according to Equation (3).

$$X_{HV}(t) = \frac{HV(t) - HV_0}{HV_\infty - HV_0} \tag{2}$$

$$X_{KV}(t) = \frac{KV_0 - KV(t)}{KV_0 - KV_\infty} \tag{3}$$

where HV_0 and KV_0 are the initial ferrite micro-hardness and impact energy in the as-solution-annealed condition, respectively. $HV(t)$ and $KV(t)$ are the ferrite micro-hardness and impact energy after aging at 475 °C (748 K) for time t [min], respectively. HV_∞ and KV_∞ are the steady-state values of the ferrite micro-hardness and impact energy in the presence of isothermal 475 °C (748 K) aging, respectively. HV_∞ is equal to 450 HV0.05 and KV_∞ is equal to 9 J. The experimental process fractions for both the ferrite micro-hardness and impact energy were modelled using the Avrami-type equation with fitting parameters a and b, as determined in Equation (4).

$$X(t) = 1 - e^{-at^b} \tag{4}$$

where t is the aging time [min] at 475 °C (748 K). The fitting parameters for both the processes were determined by the least-square procedure and the related values are shown in Table 6. The goodness of the fitting was assessed by calculating the determination coefficients, the values of which are shown in Table 6.

Table 6. Fitting parameters of the process-fraction curves based on the Avrami-type equation.

Parameter	X_{KV}	X_{HV}
a	8.47×10^{-6}	8.80×10^{-7}
b	3.3486	3.3507
R^2	0.97	0.99

The fitting curves and the experimental values for both the ferrite micro-hardness and the impact-energy process fractions are shown in Figure 11 as functions of the aging time. In accordance with the previous observations, the process–fraction curves showed the presence of different kinetics between the phenomena of ferrite hardening and impact-energy loss. The fitting parameter *a* rose, increasing the rapidity of the process in reaching the steady-state condition, while the parameter *b* rose, increasing the duration of the activation phase. The parameter *a* was higher for the process of impact-energy loss, while the parameter *b* was slightly higher for the process of ferrite hardening. This confirmed, again, that the ferrite-hardening process was delayed with respect to the impact-energy loss. Moreover, the process of the impact-energy loss reached the steady-state condition more rapidly.

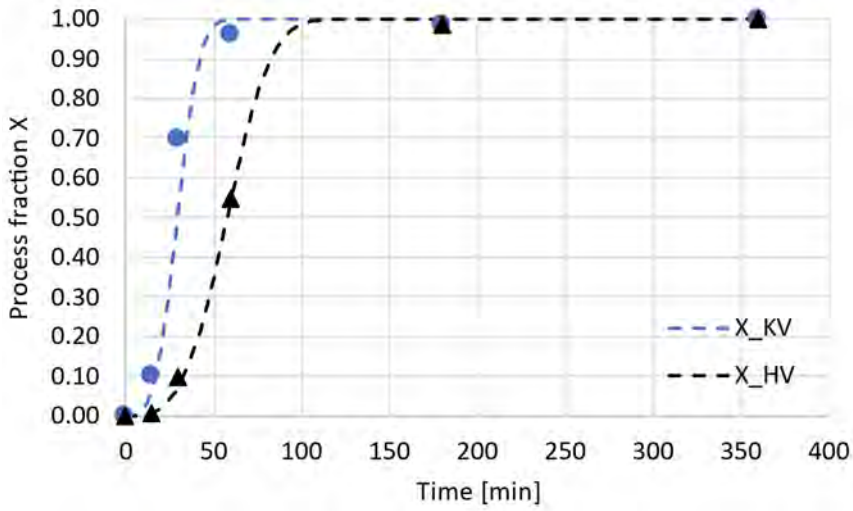

Figure 11. Hardness and impact-energy process fractions. Fitting curves and experimental values for both the ferrite micro-hardness and impact energy as functions of the aging time.

Even though the impact energy was the best parameter for investigating the ferrite spinodal decomposition, the micro-hardness test was significantly faster and cheaper. Therefore, the relationship between the ferrite micro-hardness and the impact energy at −46 °C (227 K) was modeled, using the Avrami-type equation with fitting parameters *a* and *b*, as per Equations (5) and (6).

$$KV(t) = KV_{\infty} + (KV_0 - KV_{\infty})\, e^{-a(HV(t)-HV_0)^b} \quad (5)$$

$$KV(t) = 9 + 150\, e^{-a(HV(t)-303)^b} \quad (6)$$

The fitting parameters were determined by the least-square procedure and the related values are shown in Table 7. The goodness of the fitting was assessed by calculating the determination coefficient, the value of which is shown in Table 7. The fitting curve between the ferrite micro-hardness and the impact energy is shown in Figure 12, together with the experimental values. This relationship confirmed the presence of a steep loss in impact energy with a slight increase in ferrite micro-hardness. According to the calculated fitting curve,

the reduction in impact energy was no longer compatible with the minimum NORSOK requirement (45 J) when the ferrite micro-hardness increased above 320 HV0.05 [14].

Table 7. Fitting parameters of the Avrami-type relationship between the ferrite micro-hardness and the impact energy.

Parameter	*KV = f(HV)*
a	0.1101
b	0.9010
R^2	0.99

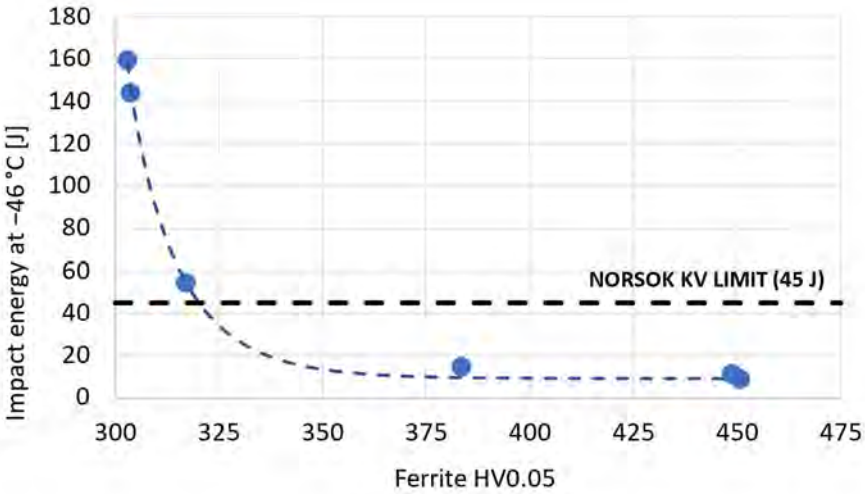

Figure 12. Fitting curves and experimental values of the impact energy as a function of the ferrite micro-hardness.

Regarding the crack-propagation path, there were no appreciable differences among the as-solution annealed and the aged conditions in terms of both the total crack length and the relative amounts of microstructural constituents. As a consequence, it is possible to state that this embrittling phenomenon and variations in the test temperature without spinodal decomposition did not appreciably influence the crack-propagation path and its microstructural constituents, even at very low absorbed impact energies, as shown in Figure 13.

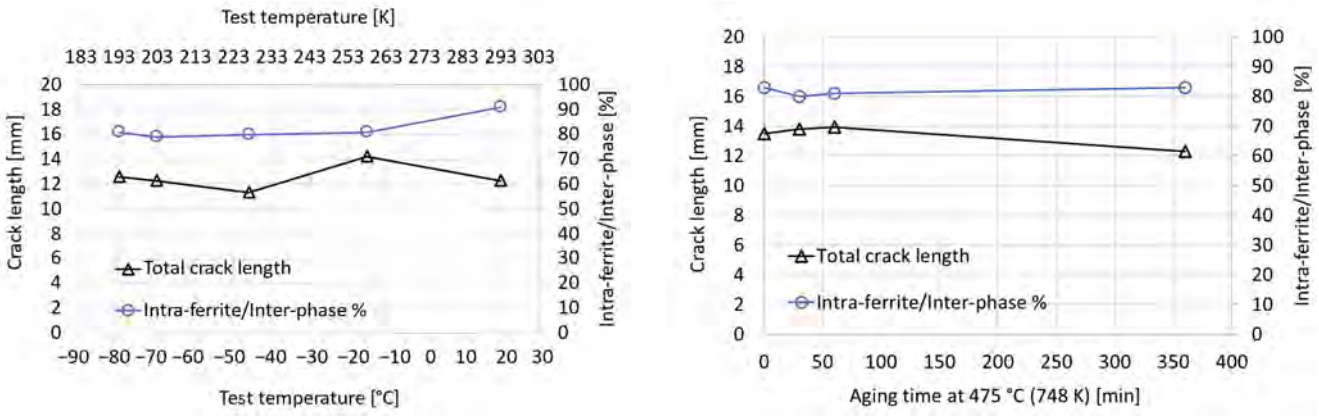

Figure 13. Crack-path length and intra-ferrite/interphase % in the Charpy impact specimens adopted to determine the ductile-to-brittle transition curve of the as-solution annealed material (**a**) and to investigate the 475 °C (748 K) embrittlement (**b**).

The major influence on the crack path was determined by the ferrite-to-austenite ratio and the microstructural arrangement (size, morphology, and distribution of the austenite islands) compared to the crack-propagation direction, as observed in the literature [6].

Regarding the impact specimens with 475 °C (748 K) embrittlement, the average crack length was equal to 13.4 mm, which was about 7% more than that of the as-solution annealed specimens (average length equal to 12.5 mm). The intra-ferrite/interphase fraction was the main one along the crack-propagation path, being an average of 82% of the overall crack-path length for both the 475 °C (748 K)-embrittled Charpy specimens and those tested to determine the transition curve.

According to the literature, the crack-propagation path follows preferentially the ferrite zones [6]. When the crack is hindered by austenite during propagation, it is forced to continue either along the interphase boundary or across the austenite island, depending on the morphology and size of the obstacle [6]. This behavior can lead to a significant deflection of the crack path out of the notch plane. The crack propagates preferably inside the regions where the required energy is lower (i.e., ferrite). When the crack deflection is excessive, it starts propagating through austenite. Such a propagation mode determines an increment in the crack-path length, even with low impact-energy values. As reported by the literature [6], the crack-propagation path strongly depends on the specimen orientation and the microstructural arrangement.

The fracture surface characteristics of the Charpy impact specimens were considered with respect to the measured impact energy at −46 °C (227 K) and compared with the findings in the literature [27–29]. In the solution-annealed condition, the fracture surface showed the presence of macro-dimples was associated with the austenite regions and both micro-dimples and cleavage facets were associated with ferrite. The austenite regions were characterized by dimples larger than those associated to ferrite, since the closely packed slip systems ensure a great deformability to austenite [6,7,30,31]. In addition, tearing ridges with small dimples were present. These ductile features were compatible with the presence of a high impact energy (159 J). They characterized most of the fracture surface, suggesting a prevalent ductile behavior at −46 °C (227 K) for the solution-annealed condition. Regarding the 475 °C (748 K)-aged conditions, after 30 min, both cleavage facets and dimples were present, suggesting the occurrence of a mixed fracture mode. Dimples mainly characterized the austenite regions, while flat low-deformation regions were associated with ferrite. Increasing the aging time, the fracture mode gradually changed from a ductile failure to a prevalent cleavage brittle failure. The embrittling effect of the ferrite spinodal decomposition was responsible for the progressive reduction in the amount and size of the dimples. After 6 h, cleavage facets became the prevalent feature, indicating a mainly brittle behavior. This was also confirmed by the significant reduction in the impact energy (15 J) [6,7,30].

The impact energy evaluated at −46 °C (227 K) after aging at 475 °C (748 K) for 30 min was equal to 54 J. The same embrittlement level could be obtained in the as-solution annealed condition, lowering the test temperature from −46 °C (227 K) to the range between −80 °C (193 K) and −70 °C (203 K). Therefore, the spinodal embrittlement phenomenon at 475 °C (748 K) determined a significant increase in the ductile-to-brittle transition curve of the material.

Regarding the fracture surfaces of the Charpy specimens adopted to determine the ductile-to-brittle transition curve, as shown in Figure 9, at −80 °C (193 K), the fracture surface was mainly characterized by the presence of cleavages. Nevertheless, tearing ridges with small dimples, associated with the austenite regions, were still present. At −46 °C (227 K), even if small cleavage zones were observed, micro- and macro- dimples mainly characterized the fracture surface. At room temperature, the fracture surface showed a ductile fracture mode with a combination of micro-dimples related to the ferrite regions and macro-dimples associated with the austenite ones.

As reported in the experimental section, the detrimental effects of the 475 °C (748 K) embrittlement on both ferrite micro-hardness and impact energy were already completely

reversed by solution-annealing at 1120 °C (1393 K) after 10 min soaking. Regarding reversion heat treatments at 600 °C (873 K) and 550 °C (823 K), both temperatures allowed only a partial recovery of ferrite micro-hardness. In fact, even though its value was reduced, at about 350 HV0.05, it was still well above the threshold level previously determined (320 HV0.05), which was required for compatibility with the NORSOK standard [14]. Therefore, these reversion treatments allowed only a partial and insufficient recovery of the initial properties. Furthermore, excessively long reversion times were not feasible at these temperatures because they could activate further precipitation phenomena, as shown by the TTP diagram in Figure 1. This is clearly demonstrated by the experimental results shown in Figure 10. In fact, after about 1 h at both 600 °C (873 K) and 550 °C (823 K), the hardness started increasing again. Therefore, long reversion times at these temperatures are not recommended, according to the precipitation response of this grade [1,8,11,12]. In conclusion, a complete reversion of the 475 °C (748 K) embrittlement was allowed only by re-solution annealing.

5. Conclusions

Biphasic stainless steels provide excellent mechanical properties, corrosion resistance, and low-temperature toughness. However, complex precipitation phenomena can occur upon thermal exposure above approximately 300 °C (573 K), with the formation of detrimental embrittling phases. Among the precipitation phenomena, the spinodal decomposition of ferrite is particularly critical in the range from 300 °C (573 K) to 500 °C (773 K). As the kinetic of this phenomenon is faster at about 475 °C (748 K), it is also known as "475 °C (748 K) embrittlement". Such transformation determines a huge toughness loss, together with a significant increase in ferrite hardness. In the technical literature, some researchers studied different methods to recover the mechanical properties after spinodal decomposition embrittlement. One proposal was represented by reversion heat treatments from 550 °C (823 K) to 600 °C (873 K). In fact, with this temperature range above the $\alpha - \alpha'$ miscibility gap in the Fe-Cr system, the decomposition became thermodynamically unstable, leading to dissolution of the α' phase. However, because of limitations on the maximum exposure time determined by the precipitation response of the material, reversion heat treatments do not allow a complete reversion of the initial pre-embrittlement mechanical properties, especially in high-chromium steel grades.

In this study, we considered a commercial cylindrical rod made of ferritic-austenitic F55-grade steel (UNS S32760), provided in as-forged condition. The samples were cut from the circumferential direction and, then, they were solution-annealed at 1120 °C (1393 K) and water-quenched. The modifications induced by the spinodal decomposition of ferrite were investigated by macro-hardness and micro-hardness tests and by Charpy impact tests, varying the soaking time at 475 °C (748 K). Upon aging at this temperature, the impact energy was rapidly reduced, leading to unacceptable values after 1 h. The influence on impact energy was observed earlier with respect to the effect on ferrite micro-hardness. Therefore, the micro-hardness method was not the most effective method to investigate the presence of spinodal decomposition, especially if the precipitation phenomenon was in its early stage.

The crack path and its relationship with the microstructure were studied by optical microscopy. As observed in this experimental study, the lengths of the crack path and its constituents were mainly affected by the specimen orientation and the microstructural arrangement, while the occurrence of the embrittlement phenomenon had no appreciable influence. The intra-ferrite/interphase fraction represented the main constituent along the crack path. Upon aging, the fracture mode gradually changed from ductile to brittle. The progressive reduction in the amount and size of the dimples and the occurrence of cleavage facets clearly demonstrated the embrittling effect of the spinodal decomposition.

The detrimental effect of the 475 °C (748 K) embrittlement was completely reversed by solution-annealing treatment at 1120 °C (1393 K). The reversion heat treatments at both

600 °C (873 K) and 550 °C (823 K) allowed only a partial recovery. Longer exposure times are not recommended because of the further precipitation of undesired phases.

Author Contributions: Conceptualization, B.R., R.G., F.T. and D.P.; methodology, R.G. and D.P.; formal analysis, R.G. and D.P.; investigation, B.R., R.G., F.T., D.P. and E.M.; writing—original draft preparation, R.G. and D.P.; writing—review and editing, B.R., R.G., F.T., D.P. and E.M.; supervision, B.R., R.G., F.T., D.P. and E.M. All authors have read and agreed to the published version of the manuscript.

Funding: This research received no external funding.

Data Availability Statement: The data presented in this study are confidential and not publicly available.

Conflicts of Interest: The authors declare no conflict of interest.

References

1. Topolska, S.; Łabanowski, J. Effect of Microstructure on Impact Toughness of Duplex and Superduplex Stainless Steels. *J. Achiev. Mater. Manuf. Eng.* **2009**, *36*, 142–149.
2. Francis, R.; Byrne, G.; Warburton, G.R.; Maligas, M.N. The selection of superduplex stainless steel for oilfield applications. In Proceedings of the Corrosion 2004, Paper n. NACE-04123, New Orleans, Louisiana, 28 March 2004.
3. Byrne, G.; Warburton, G.; Schulz, Z.; Francis, R. ZERON 100 (UNS S 32760 modified), Advanced Forging Process (AFP), Super Duplex Stainless Steel for Increased Low Temperature Impact Toughness and Resistance to Hydrogen Induced Stress Corrosion Cracking (HISCC) of API Forgings for Subsea Applications. In Proceedings of the Offshore Technology Conference, Rio de Janeiro, Brazil, 29–31 October 2013.
4. Rivolta, B.; Gerosa, R.; Tavasci, F. Heat Treatment and Impact Toughness of the F55-Grade Steel. *Mater. Perform. Charact.* **2020**, *9*, 126–138. [CrossRef]
5. Rivolta, B.; Gerosa, R.; Tavasci, F. The dilatometric technique for studying sigma phase precipitation kinetics in F55 steel grade. *J. Therm. Anal. Calorim.* **2018**, *132*, 869–877. [CrossRef]
6. Pettersson, N.; Wessman, S.; Thuvander, M.; Hedström, P.; Odqvist, J.; Pettersson, R.F.A.; Hertzman, S. Nanostructure evolution and mechanical property changes during aging of a super duplex stainless steel at 300 °C. *Mater. Sci. Eng. A* **2015**, *647*, 241–248. [CrossRef]
7. Örnek, C.; Burke, M.G.; Hashimoto, T.; Engelberg, D.L. 748 K (475 °C) Embrittlement of Duplex Stainless Steel: Effect on Microstructure and Fracture Behavior. *Metall. Mater. Trans. A* **2017**, *48*, 1653–1665. [CrossRef]
8. Danoix, F.; Auger, P.; Blavette, D. Hardening of Aged Duplex Stainless Steels by Spinodal Decomposition. *Microsc. Microanal.* **2004**, *10*, 349–354. [CrossRef] [PubMed]
9. ArcelorMittal, I. Duplex Stainless Steels Welding Guidelines. 2019. Available online: https://industeel.arcelormittal.com/wp-content/uploads/2021/03/Duplex-Stainless-Steels-Welding-Guidelines-EN-Juin-2019-Web.pdf (accessed on 25 April 2022).
10. Association, I.M. Practical Guidelines for the Fabrication of Duplex Stainless Steels. 2014. Available online: https://www.imoa.info/download_files/stainless-steel/Duplex_Stainless_Steel_3rd_Edition.pdf (accessed on 25 April 2022).
11. Shamanth, V.; Ravishankar, K.S. Dissolution of alpha-prime precipitates in thermally embrittled S2205-duplex steels during reversion-heat treatment. *Results Phys.* **2015**, *5*, 297–303. [CrossRef]
12. Shamanth, V.; Ravishankar, K.S.; Hemanth, K. Duplex Stainless Steels: Effect of Reversion Heat Treatment. In *Stainless Steels and Alloys*; IntechOpen: London, UK, 2019. [CrossRef]
13. *A182/A182M-21*; Standard Specification for Forged or Rolled Alloy and Stainless Steel Pipe Flanges, Forged Fittings, and Valves and Parts for High-Temperature Service. ASTM International: West Conshohocken, PA, USA, 2021. [CrossRef]
14. *NORSOK M-630*; Material Data Sheets and Element Data Sheets for Piping. NORSOK Standard: Lysaker, Norway, 2010.
15. *E112-13*; Standard Test Methods for Determining Average Grain Size. ASTM International:: West Conshohocken, PA, USA, 2013. [CrossRef]
16. *E407-07*; Standard Practice for Microetching Metals and Alloys. ASTM International: West Conshohocken, PA, USA, 2015.
17. *ISO 6507-1:2018*; Metallic Materials—Vickers Hardness Test. ISO: Geneva, Switzerland, 2018.
18. *A370-21*; Standard Test Methods and Definitions for Mechanical Testing of Steel Products. ASTM International: West Conshohocken, PA, USA, 2021. [CrossRef]
19. *E23-16*; Standard Test Methods for Notched Bar Impact Testing of Metallic Materials. ASTM International: West Conshohocken, PA, USA, 2016. [CrossRef]
20. *E562-19*; Standard Test Method for Determining Volume Fraction by Systematic Manual Point Count. ASTM International: West Conshohocken, PA, USA, 2019. [CrossRef]
21. Pettersson, N.; Pettersson, R.F.A.; Wessman, S. Precipitation of Chromium Nitrides in the Super Duplex Stainless Steel 2507. *Metall. Mater. Trans. A* **2015**, *46*, 1062–1072. [CrossRef]
22. Hereñú, S.; Moscato, M.G.; Alvarez, I.; Armas, A.F. The Influence of Chromium Nitrides Precipitation on the Fatigue Behavior of Duplex Stainless Steels. *Procedia Eng.* **2014**, *74*, 179–182. [CrossRef]

23. Krupp, U.; Söker, M.; Giertler, A.; Dönges, B.; Christ, H.-J.; Wackermann, K.; Boll, T.; Thuvander, M.; Marinelli, M.C. The potential of spinodal ferrite decomposition for increasing the very high cycle fatigue strength of duplex stainless steel. *Int. J. Fatigue* **2016**, *93*, 363–371. [CrossRef]
24. Chen, W.; Xue, F.; Tian, Y.; Yu, D.; Yu, W.; Chen, X. Effect of thermal aging on the low cycle fatigue behavior of Z3CN20.09M cast duplex stainless steel. *Mater. Sci. Eng. A* **2015**, *646*, 263–271. [CrossRef]
25. Haghdadi, N.; Cizek, P.; Hodgson, P.D.; Beladi, H. Microstructure dependence of impact toughness in duplex stainless steels. *Mater. Sci. Eng. A* **2019**, *745*, 369–378. [CrossRef]
26. Li, S.L.; Zhang, H.L.; Wang, Y.L.; Li, S.X.; Zheng, K.; Xue, F.; Wang, X.T. Annealing induced recovery of long-term thermal aging embrittlement in a duplex stainless steel. *Mater. Sci. Eng. A* **2013**, *564*, 85–91. [CrossRef]
27. Iacoviello, F. La resistenza alla corrosione degli acciai duplex. In *Giornata Di Studio—Acciai Inossidabili Duplex*; Associazione Italiana di Metallurgia: Milan, Italy, 2003.
28. Biezma, M.V.; Berlanga, C.; Argandona, G. Relationship between microstructure and fracture types in a UNS S32205 duplex stainless steel. *Mater. Res.* **2013**, *16*, 965–969. [CrossRef]
29. Mililitsky, M.; Matlock, D.K.; Regully, A.; Dewispelaere, N.; Penning, J.; Hanninen, H. Impact toughness properties of nickel-free austenitic stainless steels. *Mater. Sci. Eng. A* **2008**, *496*, 189–199. [CrossRef]
30. Li, S.; Wang, Y.; Li, S.; Zhang, H.; Xue, F.; Wang, X. Microstructures and mechanical properties of cast austenite stainless steels after long-term thermal aging at low temperature. *Mater. Des.* **2013**, *50*, 886–892. [CrossRef]
31. Sahu, J.K.; Krupp, U.; Ghosh, R.N.; Christ, H.-J. Effect of 475 °C embrittlement on the mechanical properties of duplex stainless steel. *Mater. Sci. Eng. A* **2009**, *508*, 1–14. [CrossRef]